



Modeling of Pulsating Inverted Conical Flames: a Numerical Instability Analysis

Louise da Costa Ramos, Luís Fernando Figueira da Silva, Florent Di Meglio,
Valéry Morgenthaler

► To cite this version:

Louise da Costa Ramos, Luís Fernando Figueira da Silva, Florent Di Meglio, Valéry Morgenthaler. Modeling of Pulsating Inverted Conical Flames: a Numerical Instability Analysis. Combustion Theory and Modelling, 2022, pp.260-288. 10.1080/13647830.2021.2011961 . hal-03322442

HAL Id: hal-03322442

<https://hal.science/hal-03322442>

Submitted on 19 Aug 2021

HAL is a multi-disciplinary open access archive for the deposit and dissemination of scientific research documents, whether they are published or not. The documents may come from teaching and research institutions in France or abroad, or from public or private research centers.

L'archive ouverte pluridisciplinaire **HAL**, est destinée au dépôt et à la diffusion de documents scientifiques de niveau recherche, publiés ou non, émanant des établissements d'enseignement et de recherche français ou étrangers, des laboratoires publics ou privés.



Distributed under a Creative Commons Attribution - NonCommercial 4.0 International License

Modeling of Pulsating Inverted Conical Flames: a Numerical Instability Analysis

Louise da Costa Ramos^{a,c}, Luís Fernando Figueira da Silva^b, Florent Di Meglio^c and Valery Morgenthaler^a

^aAnsys Fr, 35-37 Rue Louis Guérin, Villeurbanne, France; ^bPontificia Universidade Católica do Rio de Janeiro, R. Marquês de São Vicente 225, 22.451-900, Rio de Janeiro, Brazil; ^cMINES ParisTech, 60 Boulevard Saint-Michel, Paris, France

ARTICLE HISTORY

Compiled May 17, 2021

ABSTRACT

The study of combustion-thermoacoustic instabilities is a topic of interest in the development of engines. However, the modeling of these systems involves a high computational burden. This paper focuses on a simpler class of systems that still features such instabilities: inverted conical flames anchored on a central bluff-body. Here these flames are modeled by solving species mass momentum and energy transport equations, coupled with a skeletal methane/air chemical kinetic mechanism. The aim is to characterize the dynamic behavior of inverted conical flames, both due to their natural dynamics and to external incoming velocity fluctuations. The main contribution is the detailed model of the flames, including the smallest scales. The analysis of the impact of the mesh adaption on the flame response shows a trade-off between model accuracy and computational burden that can be adjusted by changing the temperature gradient threshold. The flame response analysis in terms of the temperature and OH mass fraction gives a detailed characterization of the flame front behavior in its different scales, both in time and space. The analysis of the flame front dynamic response employing FFT shows that these have a natural frequency of 35 *Hz*, and this frequency interacts with the flame response due to incoming velocity excitations. More specifically, when forcing the flame with low frequencies ($f \leq 125$ *Hz*) the flame responds only to the forcing and some harmonics, whereas when forcing between $125 < f \leq 172$ *Hz* the flame response comprises both the natural and forced behavior. Forcing beyond 200 *Hz* shows the natural flame response only.

KEYWORDS

laminar premixed flame; thermo-acoustic instability; flame transfer function; flame frequency response; computational fluid dynamics

1. INTRODUCTION

Combustion modeling is a powerful tool for the analysis of simple systems, such as domestic boilers, and more complex devices, such as gas turbine combustors. In several of those systems, the combustion and thermoacoustic coupling may cause flow

CONTACT L. da Costa Ramos. Email: louise.ramos@ansys.com

CONTACT L. F. Figueira da Silva. Email: luisfer@puc-rio.br

CONTACT F. Di Meglio. Email: florent.di_meglio@mines-paristech.fr

CONTACT V. Morgenthaler. Email: valery.morgenthaler@ansys.com

perturbations on the flame, which in turn can lead to unstable behaviors. The design of those practical systems heavily relies on computational fluid dynamics models (CFD), thus avoiding the cost of experiments. In cases where flow perturbations may arise, three dimensional unsteady simulations, involving multiple chemical species, as well as as the associated time scales, are often necessary in order to built an adequate model [1–3]. In recent years, the computational power increase has allowed a large number of such detailed simulations, thus enabling the design of novel combustors.

Lean premixed flames are known to exhibit unstable behavior in low emission systems [4, 5]. Therefore, to understand the physics of flame response to incoming velocity/pressure perturbations, several studies have been performed, both in combustors and laboratory flames [6]. Accordingly, investigations on flame instabilities carried on complex combustors [7, 8], have shown that mechanisms involving fuel/air equivalence ratio fluctuations that triggered by pressure oscillations at the injector exhaust, vortical/flame roll up, and that these interactions with hydrodynamic instability modes might be driving sources of unsteady motion [8, 9]. Laminar premixed inverted conical flames, which are anchored on a central bluff-body, however, feature instability phenomena with a rather simple flow field framework. Accordingly, studies have been developed on this flames, either based on laboratory [4, 10], or on CFD models [9]. More specifically, the instabilities characterizing the inverted conical flames have been shown to be caused by flow velocity fluctuations that couple with the flame and generate thermoacoustic instabilities. These phenomena may be studied by exciting the flame with forced velocity oscillations at a specific frequency and magnitude. Thereby, the inverted conical flame is also representative of more complex situations, such as gas turbines combustors, enabling the further understanding of the combustion coupling with acoustics [11]. A synthetic description of the flame response to velocity fluctuation is the Flame Describing Function, which can be experimentally characterized [10] and thus can be used to predict instabilities.

Standard laminar conical flame dynamical instabilities have been extensively studied [12–15]. The flame front dynamics of a inverted conical flame has been analyzed for a confined flame [14], and the non-linear response of ducted flames anchored on a central rod has also been addressed [15]. However, to the best of the authors knowledge, few modeling studies exist concerning laminar premixed inverted conical flames anchored on a bluff-body [9, 10], or the computational study of the flame response due to forcing, which is the aim of this paper, and the corresponding characterization of the thermoacoustic instability behavior.

Therefore, in this paper a laminar axisymmetric premixed inverted conical flame (ICF) is analyzed on a burner which has cylindrical rod on its center. In Fig. 1 this flame position is represented by the computed instantaneous mass fraction field of OH, enabling the verification of the flame anchoring point on the central rod, and the overall inverted conical behavior. Classically, the premixed flame front separates the fuel/air mixture from the combustion products. This flame has been shown to be susceptible to thermo-acoustic instabilities, mainly driven by flame convective vorticity mode [10]. This instability may be seen at the vicinity of tip of the flame in Fig. 1, and will be discussed in this paper. The same flame and setup has already been modeled and analyzed in its steady state [9], where the flame was shown to exhibit a pseudo steady state behavior.

The characterization of the response of flames to incoming excitation has been an interesting research topic on the past decades. For instance, the analytical study of a model of a transversely forced flame on a two-dimensional Bunsen flame under transverse mean flow has underscored the influence of several effects, such as frequency,

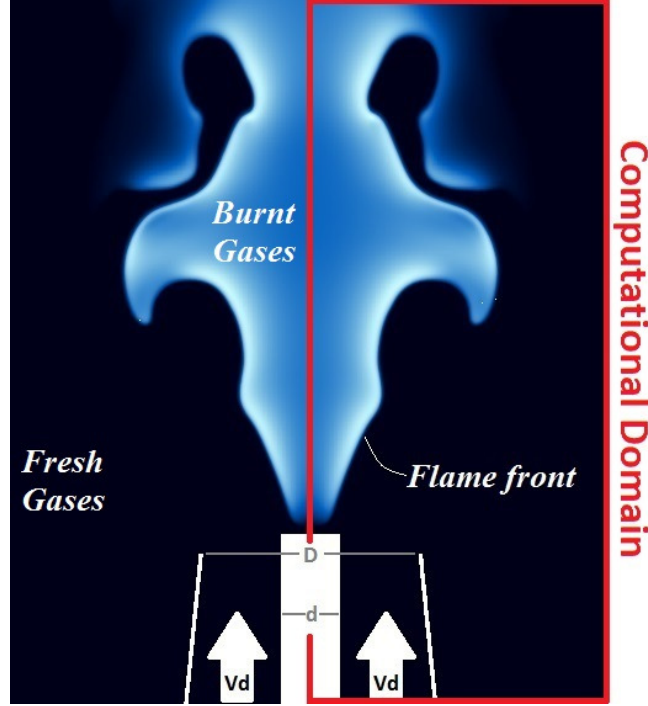


Figure 1.: Representative view of OH mass fraction for the unsteady inverted conical flame. Mean velocity of $v_d = 2.05 \text{ m/s}$ and methane/air equivalence ratio $\phi = 0.92$.

transverse mean flow velocity and vertical mean flow velocity on the Flame Transfer Functions (FTFs) [16]. Studies of laminar premixed V-flame forced with high frequency [17] have shown that the acoustic transverse standing wave response depends on the acoustic condition, having two response patterns; pairing process where multiple-vortex interact in the jet outer layer, or a helical mode in the inner layer behind the rod. Analyses of the dynamic response of premixed flames have also been experimentally performed with chemiluminescence cross-correlation maps [18, 19]. Moreover, results [18] have shown consistency with physical interpretation proposed for the cross-correlation maps, confirming its potential for diagnosing the effective contribution of different flame regions to the global dynamic response. The dynamics of the flame leading edge in a laminar premixed flame stabilized on a bluff body in a channel have been described also [19]. The identification of FTFs in the presence of intrinsic thermoacoustic feedback and noise by applying LES and system identification approach was used to model turbulent reacting flow under broadband excitation [20]. A coupled FDF with a neural network thermoacoustic approach, over an LES model of a turbulent and partially premixed flame led to the prediction of combustion instability limit cycle oscillations [21]. By applying steady flamelet model and the flamelet/progress variable approach, a computational analysis of the coupling of transient flame dynamics was effected, such as the local extinction and the thermoacoustic instability, in self-excited resonance combustor, enabling the identification of mechanisms of thermoacoustic instability [22]. Recent studies on the FTF in premixed flame dynamics analyzed the significant impact of the flame geometry into its acoustic response [23], and modeled the premixed flame linear dynamics in terms of time delays [24], thus

characterizing an acoustically compact flame by its impulse response, enabling for the development or control techniques in the combustion and thermoacoustic domain.

This paper is thus devoted to study the dynamics of the axisymmetrical, laminar premixed inverted conical flames, anchored on a cylindrical rod, with external dilution by air. This characterization is based on a computational fluid dynamics (CFD) model, enabling the analysis of the flame response to a variety of flow velocity forcing, thus aiming to achieve a dynamic approximation of the unsteady inverted conical flame and the associated thermoacoustic response by means of flame transfer function.

The main contribution of this work is the detailed model of a laminar premixed inverted conical flame, such that not only the main characteristic of the flame are described, but also its small scale internal behavior. The use of a skeletal chemical kinetic models enables the characterization of the flame internal structure in terms of various flame properties, such as temperature, velocity and mass fraction of several species, its natural dynamics and the flame transfer function.

This manuscript is organized as follows; first, the computational model of the ICF is defined, thus describing the computational domain, its geometry and mesh. Second, the simulation scenarios and the output scenarios are defined. Subsequently, a frequency domain analysis is defined, which will be used to characterize the thermoacoustic response of the flame. Then, the analysis of the impact of the mesh adaptation over the flame dynamic response is presented. Finally, the ICF dynamic model results are presented for two different cases; the unforced flame and the forced flame, where the first one model the ICF natural dynamics, and the other model the flame response to an incoming forcing.

2. NUMERICAL METHODOLOGY

In this section, the methodology used to model the dynamics of the ICF with Fluent 2019R3/2020R1 is presented.

2.1. Computational Fluid Dynamics

Figure 2 presents the dimensions and boundaries of the computational domain considered. The ICF modeled here is based on the study of [9, 10], with a burner outlet diameter of $D = 22 \text{ mm}$, fed with a lean methane-air mixture (equivalence ratio $\phi = 0.92$). The premixed fuel enters in the mixture-inlet, whereas air enters in the air-inlet with a small velocity of $v_{air} = 0.3 \text{ m/s}$, ensuring that the air flow in the domain moves downstream. The flame is anchored on a central rod with a diameter of $d = 6 \text{ mm}$ that is 2 mm higher than the burner outlet. Note that the chosen computational domain longitudinal dimensions are larger than the flame longitudinal dimension, $\approx 80 \text{ mm}$ measured with Fluent rule, which ensures that the flame inherent behavior is not influenced by this dimension. In this paper the fuel/air inlet flow has a fluctuating volume flow rate (\dot{V}_d), and thus, a variable mean flow velocity, v_d , and constant ambient pressure and temperature of 1 atm and 300 K , respectively.

The model of the ICF is solved using Ansys Fluent 2019/2020. Some problem setups are performed prior to the combustion model: define the geometry, the mesh and the boundary conditions. Since the flame is laminar and axisymmetric, the domain is composed of a 2D slice. The axisymmetric system has eleven boundaries, where six are walls, two inlets, one outlet, one axis and one slip boundary, as shown in Fig. 2. The non-slip walls inside of the burner are W_1 and W_2 , whereas the externals are W_5

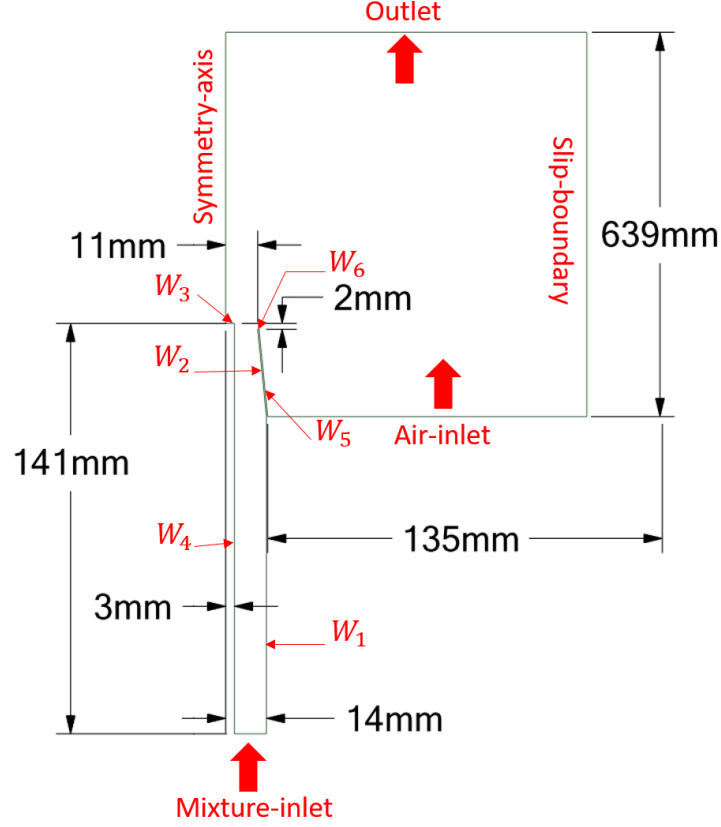


Figure 2.: Representation of the axisymmetric computational domain with corresponding internal dimensions and boundary conditions. The domain longitudinal extension is of 730 *mm*.

and W_6 , the centered bluff-body walls are W_3 and W_4 , and the *Slip – boundary* represents an open confinement. The *outlet* is prescribed the pressure outlet, and the *axis* represents the symmetry of the system. The *mixture – inlet* and the *air – inlet* are prescribed velocity inlets, with variable velocity and $v_{air} = 0.3 \text{ m/s}$, respectively. Further information about the mesh and the domain divisions can be found in [9].

The ICF is modeled here using the unsteady transport equations of species mass, momentum and energy in an axisymmetric reference frame. The species mass transport equation accounts for multi-species diffusion coefficients, the Soret thermodiffusion effects, the Fick’s law of diffusion, but the hypothesis of isobaric flame allows neglecting the barodiffusion effects. The energy transport equation accounts for the non-unity Lewis number effects, but neglects thermal radiation since it is a lean premixed flame, which does not exhibit soot formation. Therefore, participating medium emission and absorption rely on H_2O and CO_2 at the burned gases only, which are significantly smaller than the convective heat transfer contribution. As a consequence, the flame may also be considered transparent regarding the thermal radiation absorption process. The momentum transport equation considers the buoyancy effect, and Newtonian fluid behavior is assumed. Regarding the transient formulation, an implicit second order model is applied.

The chemical kinetic process for the mixture is described by the DRM19 [25] skeletal model, which is composed of 19 (plus N_2) species and 84 reactions. Previous studies

with chemical kinetic models support this choice for the considered ICF [9, 26].

Regarding the basic characteristics of the inverted conical flame studied here, for the skeletal chemical model DRM19 [25], the ICF is characterized by a flame adiabatic temperature of $T_{ad} = 2,200\text{ K}$, a laminar flame speed (S_L) of 40 cm/s , a flame front thickness of $120\text{ }\mu\text{m}$, thus leading to a minimum necessary mesh size required of $5.6\text{ }\mu\text{m}$ [9]. However, the minimum mesh size necessary is too small to be used in the whole domain, as it would result in a too large number of computational mesh nodes, and thus to a heavy computational burden. Therefore, here a baseline characteristic mesh of $100\text{ }\mu\text{m}$ is used, which has been chosen to guarantee that, initially, at least one computational mesh node is positioned within the flame front. A mesh adaptation tool is used to reduce the mesh size from $100\text{ }\mu\text{m}$ to the minimum required ($5.6\text{ }\mu\text{m}$), only in the regions where reactions occur, i.e., where a high temperature gradient is found. An analysis of the impact of the impact of the mesh refinement parameters is performed in section 2.5.

2.2. Simulation Scenarios

In this paper, two dynamic simulation scenarios are considered. First, a constant fuel/air mean inlet velocity of $v_d = 2.05\text{ m/s}$ is imposed which enables the analysis of the unforced flame dynamics. Then, the flame is excited by an external mean velocity forcing, of the following form

$$v_{mix}(t) = v_d + v(t), \quad v(t) = v_a \cos(2\pi ft), \quad (1)$$

where v_a is the excitation amplitude, and f its frequency in Hz . This enables the analysis of the flame response and the characterization of the flame describing function (FDF) [6]. More specifically, the forced case which is here described has root mean square velocity of $RMS(v_a) = 0.14\text{ m/s}$ and a frequency ($f [\text{Hz}]$) which is the parametric variable of the study. The values are chosen based on those experimentally used [10], which indicate that this set yields the maximum response gain for the inverted conical flame. In Section 3, the results of the unforced and forced cases are presented and discussed.

2.3. Outputs of Interest

To study the time evolution of some of the computed reactive flow properties, twenty analysis points are placed in the flame fluctuation region. These points span four horizontal lines along the flame height ($z = \text{constant}$), each containing five points, as shown in Fig. 3. Their coordinates are empirically chosen such that, at any time and for any shape of the ICF, there is at least one measurement in each of the following important regions: the fresh gases, the reactive region or flame front and the burned gases. In Fig. 3, these data extraction points are superimposed on the flame front, each labeled from A to T . The coordinates of these points in the normalized (z, r) plane are presented in Tab. 1. The model provides a variety of flame properties to be analyzed: mass fraction of CH_2 , H , OH , H_2O , density, velocity, etc. Here, for the sake of brevity, only the time variations of temperature (T), pressure (P) and OH mass fraction (Y_{OH}) are presented and discussed. This data serves two main purposes : (i) the characterization of the flame time and spatial scales, and (ii) the analysis of its

acoustic response, through the pressure and flame surface area fields.

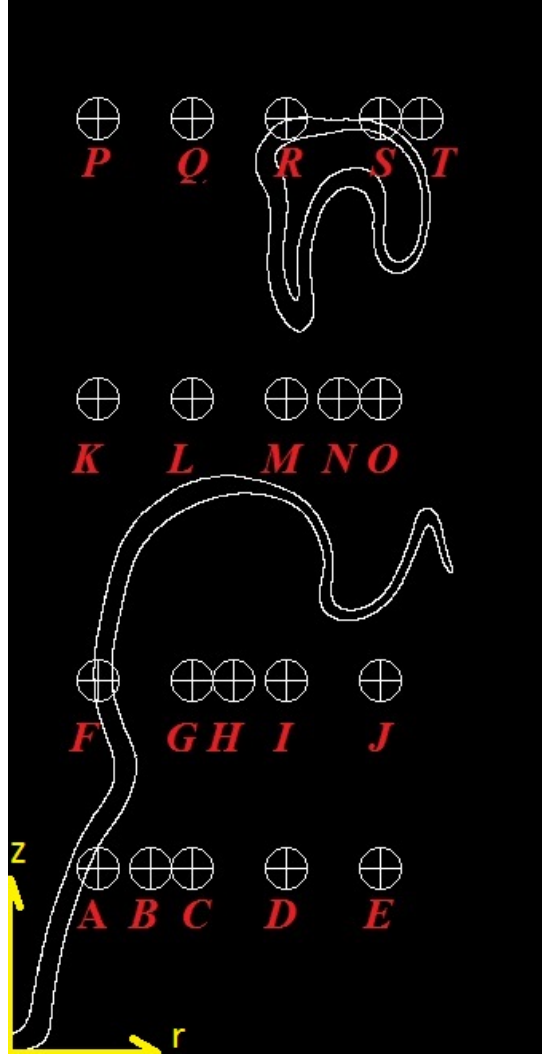


Figure 3.: Data extraction points.

Table 1.: Point name and corresponding (z^*, r^*) non dimensional coordinates of each point shown in Fig. 3. These are non dimensional axial and radial coordinates, such that $z^* = z/D$ and $r^* = r/D$, where $D = 22 \text{ mm}$ is the *mixture – inlet* tube outlet diameter.

A	B	C	D	E
(0.41, 0.20)	(0.41, 0.32)	(0.41, 0.41)	(0.41, 0.61)	(0.41, 0.82)
F	G	H	I	J
(0.82, 0.20)	(0.82, 0.41)	(0.82, 0.50)	(0.82, 0.61)	(0.82, 0.82)
K	L	M	N	O
(1.43, 0.20)	(1.43, 0.41)	(1.43, 0.61)	(1.43, 0.73)	(1.43, 0.82)
P	Q	R	S	T
(2.05, 0.20)	(2.05, 0.41)	(2.05, 0.61)	(2.05, 0.82)	(2.05, 0.91)

2.4. Frequency domain analysis

This work focuses on two physical quantities of interest to analyze the harmonic behavior of the flame. First, the pressure data from the measurement points presented in Tab. 1 are processed. Second, the computation and analysis of the evolution of the flame surface area is done, to determine the FTF.

2.4.0.1. Pressure post-processing. the raw pressure data $P(t)$ is analyzed in the frequency domain by applying a Fast Fourier Transform (FFT) [27]. Then, the frequencies are filtered with a simple square window filter, so that the computational noise is removed. Indeed, since the time step of the model is $\Delta t = 100 \mu s$, a noise of frequency of $f = 10 kHz$, or one of its harmonics, may be present in the CFD results. One may note that this noise frequency is around 100 times higher than the characteristic flame frequencies studied on this paper, which are smaller or equal to $f = 1 kHz$, thus allowing the window filter to remove all frequencies beyond this value, without compromising the expected physical response.

2.4.0.2. Flame surface area. the flame surface area is obtained from the CFD results to characterize the Flame Transfer function (FTF). It should be noted that a flame surface area may not be unambiguously defined from the reactive flow properties. Therefore, to compute the flame surface area, it is necessary to, first, chose which of the modeled flame properties is used to approximate the flame front, in a comparable way to experiments. For the ICF model computed with a DRM19 kinetic model, the CH_2 mass fraction is assumed to yield a fair representation of the flame front shape and thickness, since its a substance produced and consumed in the reactive region [9]. Thus, to define the flame surface from the CH_2 mass fraction field (Y_{CH_2}), a binary variable α is defined, such that at each location x and time t , $\alpha(x, t)$ is defined as;

$$\alpha(x, t) = \frac{\psi(x, t) + 1}{2}, \quad \psi(x, t) = \frac{\delta(x, t)}{(|\delta| + \epsilon)}, \quad \delta(x, t) = Y_{CH_2}(x, t) - \frac{Y_{CH_2}^{max}}{\sigma}, \quad (2)$$

where, $\epsilon = 10^{-16}$ is the machine zero, $Y_{CH_2}^{max} = 6.25 \times 10^{-7}$ is the computed maximum CH_2 mass fraction within the unperturbed flame and σ is a constant that controls the flame front resulting thickness.

The result of this transformation is depicted in Fig. 4. Different choices of the parameters defining α in Eq. (2) have been explored. The choice of parameters for Eq. 2, such as $Y_{CH_2}^{max}$, were made enabling the binary flame surface area to yield a flame front thickness of $\approx 120 \mu m$, i.e., the flame thermal thickness [9]. In this case, $\sigma = 10$ is used to obtain this flame thickness.

The isosurface of each of the $\alpha(x, t)$ fields is then used, to obtain the instantaneous flame surface. Accordingly, a search for every cell of the computational domain which has a value of $\alpha = 1$ is done, and the values found characterize the borders of the flame front. Then, the surface coordinates are integrated to compute the area of the flame surface, and this value is further used to approximate the flame front surface area (A). One may note that, since a two dimensional model is used, the isoline $\alpha = 1$ is obtained.

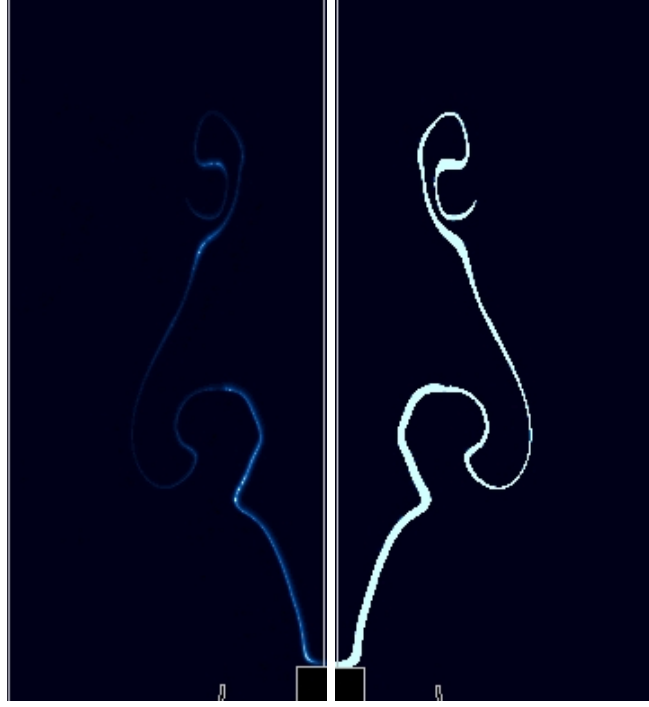


Figure 4.: Comparison of flame front with the CH_2 mass fraction (left) and with the binary field α (right).

2.4.0.3. Flame Transfer Function (FTF). The heat release rate plays a pre-dominant role in the onset of the thermoacoustic instabilities. Its harmonics response to velocity fluctuations characterizes the so-called Flame Transfer Function (FTF) [6, 12, 13, 28], that is defined as the ratio of the relative heat release rate fluctuation (Q') over the relative velocity fluctuation (v') in the frequency domain. These heat release fluctuations (Q') are here assumed to be proportional to those of the flame surface area (A') [29], such that the FTF is defined as:

$$F(f) = \frac{A'(f)/\bar{A}}{v'(f)/\bar{v}}, \quad (3)$$

where \bar{A} and \bar{v} are the mean values of the flame surface area and of the velocity, respectively. One should note that such an approximation is similar to performed in the experiments, where CH^* chemiluminescence is assumed to represent the heat release rate. The FTF can also be expressed in terms of gain (G) and phase (φ), such that the gain reflects the magnitude flame response and the phase defines the lag between the velocity and flame surface area fluctuation, as presented in the following equation:

$$F(f) = G(f)e^{i\varphi(f)}. \quad (4)$$

2.5. Influence of the mesh adaption

In this section, the impact of the computed mesh adaption is discussed, since this purely numerical effect directly impacts the flame dynamic behavior. The effect of the trade off between accuracy and computational burden is illustrated here, and a choice of parameters well suited to our objective is proposed.

The main adaption strategy comprises two degrees of freedom, which are the refinement and coarsening temperature gradients, and those are varied into different thresholds such that an highly and a poorly refined mesh are compared. Their impact on the accuracy of the computations is characterized by performing four simulations under a forcing frequency $f = 100 \text{ Hz}$, which is where the highest FTF gain have been found in experiments [10]. The two degrees of freedom are the temperature gradients thresholds for coarsening and refining, respectively. The values used for each simulation are presented in Tab. 2. This particular set of parameters has been chosen to encompass a very poorly refined mesh up to an excessively refined mesh. Indeed, a typical value for the laminar flame thickness is $100 \mu\text{m}$, and the corresponding temperature increase is $1,500 \text{ K}$, to which implies a maximum temperature gradient of $\sim 10 \cdot 10^6 \text{ K/m}$. Considering that the maximum number of allowed refinement steps is 12, the minimum resulting mesh spacing that can be obtained, if 12 refinement steps are used, is $0.7 \mu\text{m}$. Also, note that the base mesh has 512,612 nodes in its initial state, and this number increases as the mesh is adapted.

Table 2.: Mesh adaption temperature gradients thresholds influence.

-	Adaption Thresholds [K/m]		Resulting mesh characteristics		
Case	Refine	Coarse	Added nodes	Estimated wall clock time cost [days/s]	Harmonic [Hz] characteristic
1	10	300	162,838	64	40; 100
2	25	400	86,016	21	100
3	50	500	43,332	11	100
4	100	600	23,146	9	100

A qualitative appraisal of the adaption strategy on the resulting mesh may be achieved by examining Fig. 5, which shows the refined mesh region in red, for one arbitrary instant of the simulation. The refined region span decreases as the temperature gradient refinement threshold increases. The adapted mesh, which is controlled by the temperature gradient, has its nodes positioned only at the regions of high temperature gradient, which also characterizes the combustion region. The typical thickness of the refined region decreases from $3,100 \mu\text{m}$ to $900 \mu\text{m}$ as the refinement threshold increases from 10 to 100 K/m . Besides this increase of the mesh adapted region, the typical number of mesh points along the flame thickness increases from 2 at the base mesh, to 16 at the most refined mesh. Indeed, the number of added mesh nodes after the first adaption is given in Tab. 2, followed by the wall clock time necessary to compute one second of the flame and the characteristic frequencies encountered of the ICF as well. The sheer influence of the refinement threshold on the computational time is evident in this table. Halving this threshold from 100 to 50 K/m induces a cost increase of 33%, whereas the subsequent halving doubles the cost. The final threshold

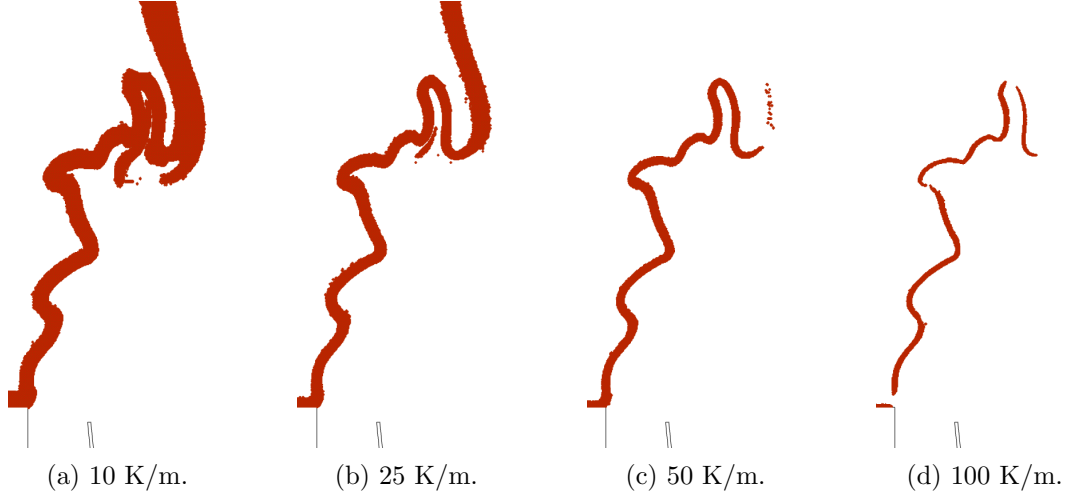


Figure 5.: Mesh instantaneous adaption region for different refinement temperature gradient values.

variation attempted, i.e., from 25 to 10 K/m is seen to correspond to a three fold increase in cost. Actually, the increasing wall clock time cost effect is directly linked to the increase of the number of mesh nodes during the simulation, since the smallest refinement gradient of 10 K/m demands the addition of four times more nodes at the first mesh adaption than when a gradient of 50 K/m is used. Note also that the number of refinement levels is practically constant as the refinement threshold decreases. For instance, the mesh actual number of levels varies between four and five for both the coarsest and the finest meshes. This has a direct consequence on the minimum mesh spacing and, thus, on the maximum time step allowed. Indeed, the mesh adaptation enables to decrease the minimum mesh size from 100 μm at base characteristic mesh, to 3.7 μm , with 5 refinement levels, at the reactive region. Nevertheless, the decrease of the mesh temperature refinement gradient threshold leads to an increased computational burden mostly linked to the increase of the size of the region of mesh adaption. One must also keep in mind that the number of added nodes to the base mesh varies during the simulation, depending of the threshold and the flame dynamics. It should be also stressed that performing a systematic frequency analysis requires a trade-off between computational cost and flame feature representation.

To further characterize the mesh adaption influence on the computed ICF, Fig. 6 depicts the flame front position, at an identical arbitrary instant, distinct from that of Fig. 5, using the different thresholds given in Tab. 2. In this figure the flame front is defined as explained in section 2.4, Eq. (2). This figure indicates that the temperature gradient threshold used for mesh refinement yields a similar flame front behavior. Indeed, the flame base exhibits a wide V-shape and the flame tip shows a similar roll-up, which is underscored by comparing Figs. 6b, 6c and 6d. Note that when using the largest refinement threshold, 100 K/m , depicted at Fig. 6d, a few discontinuities along the flame front arise. These are artifacts of the binarization procedure and do not represent physical behavior, but indicate that such a large refinement threshold is insufficient to describe the flame surface. However, when a temperature gradient refinement threshold of 10 K/m is used, the flame front presents a somewhat different behavior, as depicted at Fig. 6a. In this particular case, the tighter mesh adaption modifies the flame base shape, tip and roll up behavior, i.e., the flame shows a narrow

V-shaped base and a premature rolling up. This analysis then, suggests that the adaption spanning from 10 to 50 K/m is capable to describe the overall flame structure, in particular the flame base shape.

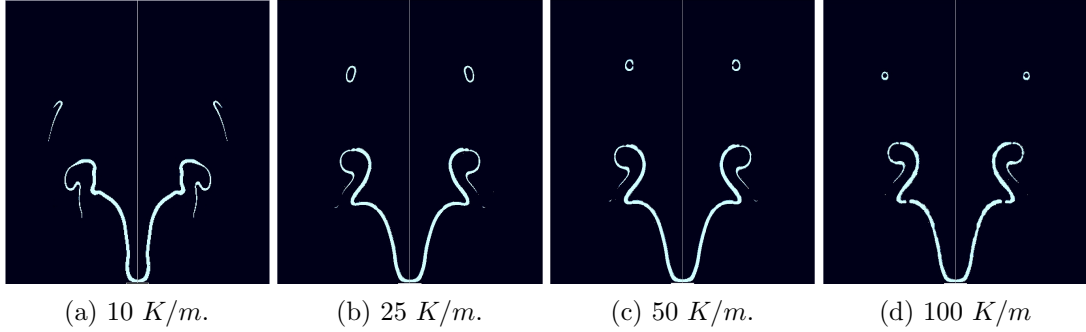


Figure 6.: Instantaneous of the flame front (α) for different mesh refinement temperature gradients thresholds.

The flame surface area fluctuations, computed as explained at section 2.4, is depicted in Fig. 7 to illustrate the impact of the thresholds on the flame front. In addition, a frequency analysis for each of the thresholds is given at Tab. 2. This figure and Tab. 2 underscore the trade-off between flame surface features representation and the corresponding cost. It is clear that choosing the tighter refinement approach of 10 K/m leads to a richer flame surface area behavior, but at the expense of significant cost. As the refinement threshold is increased, the flame surface variations are certainly less complex. More precisely, for the refinement threshold of 10 K/m , the normalized flame surface fluctuations present a maximum oscillation amplitude of approximately ± 0.5 (Fig. 7a), and the fluctuation behavior corresponds to two main frequencies of 100 Hz and 40 Hz , the first of which corresponds to the forcing frequency. The smaller frequency is absent from the flame surface fluctuations observed for the three larger refinement thresholds, which retain the forcing frequency only, with a smaller normalized surface area amplitude, of ± 0.4 . Thus, even if the 100 K/m adaption approach is seen not to reproduce the flame surface details adequately, the overall forcing frequency response is obtained.

In order to summarize the results of this section and provide comparison with the experimental results [10], Fig. 8 presents the Root-Mean-Square (RMS) of the flame surface area fluctuations and the corresponding FTF gain, defined by Eq. (4), as a function of the refinement threshold. This figure shows that both these quantities decrease simultaneously when the mesh adaption is tighter. Indeed, when the temperature gradient refinement threshold is either 50 or 100 K/m , $RMS(A') \approx 0.3 \text{ m}^2$ and the gain is close to 2.1. The gain has a value of around 1.5 for the thresholds of 10 and 25 K/m , and the corresponding $RMS(A') \approx 0.15 \text{ m}^2$. The computed mean flame surface area, the RMS velocity and mean velocity have a constant dependency of the refinement gradient, and its corresponding values are 0.0132 m , 0.2 m/s and 2.31 m/s , respectively.

The experimental results [10], obtained for identical forcing, present a gain of 1.5, which is the same value obtained here for the refinement threshold of 10 K/m or 25 K/m . However, as already seen at Tab. 2, at least three months are necessary to model 1.5 s of the dynamics of the ICF using a refinement gradient of 10 K/m , which is around six times the time necessary to perform the same computation but using 50 K/m . As a consequence, a parametrical analysis of the frequency influence

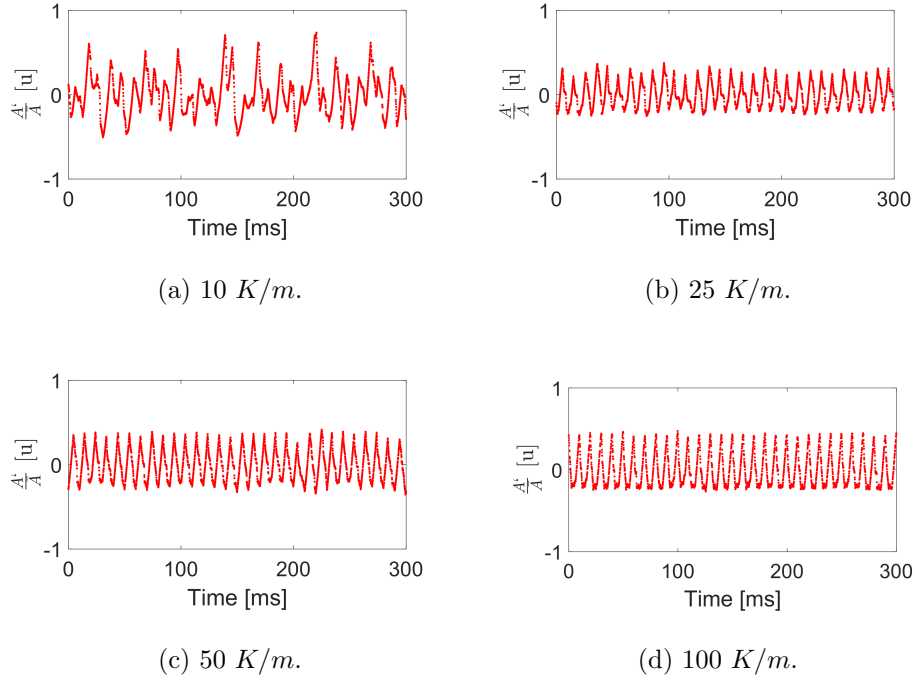


Figure 7.: Flame surface area fluctuations results for each of the cases presented at Tab. 2, i.e., different refinement thresholds.

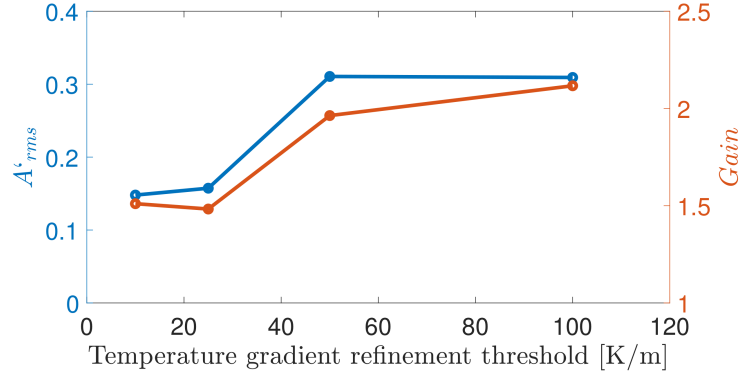


Figure 8.: RMS values of the flame surface area fluctuation [m^2] and the corresponding FDF gain as a function of the temperature gradient refinement threshold.

on the flame behavior could not be performed using the tighter refinement approach of 10 K/m . For this reason, a threshold value of 50 K/m is used in what follows for the forced ICF. Although this result is an overestimation of the gain, the qualitative response of the flame can still be assessed.

3. RESULTS AND DISCUSSION

In this section, the description and discussion of the numerical simulations corresponding to the unforced and excited scenarios are presented.

First, the unforced flame results are given in Section 3.1, where the characterization of the ICF overall flame structures, the inherent fluctuating temperature and OH mass fraction in Sections 3.1.1 and 3.1.2, are respectively given. Finally, the excited flame response is discussed in Section 3.2, where the fluctuating forced flame structures, the frequency analysis of the flame surface area fluctuation and the flame describing function in Sections 3.2.1, 3.2.2 and 3.2.3, are respectively presented.

All the simulations presented here were developed in parallel, with Linux-64 SuSE, Intel(R) Xeon(R), at Ansys cluster, using between 100 to 180 nodes to run Fluent.

3.1. Unforced flame analysis

In this section the analysis of the unforced ICF is developed. The aim is to characterize the flame structure, as well as the surface area and pressure fluctuations in such a naturally unsteady case. This enables the comparison with forced flames, in section 3.2. Since this is the single unforced case analyzed, and in order to capture the flame dynamics, the adaption refinement threshold gradient chosen is of $10\text{ K}/m$.

3.1.1. Overall flame structures

The unsteady flame model is able to describe several instantaneous flow properties. Here, in order to assess the ICF natural unsteady behavior, the flame front position is depicted using the field of α defined by Eq. (2). Accordingly, Fig. 9 shows the instantaneous flame front at different times, regularly spaced by $100\text{ }\mu s$. This particular set of images has been chosen so as to represent a full cycle of natural flame oscillation. For the sake of the present structure discussion, the flame may be divided in three different regions, from upstream to downstream. The flame surface may be seen to exhibit distinct behaviors at each of these three regions; one at the vicinity of the central rod stabilization, another at the second third, where the roll up occurs, and the last at the freely standing flame tip, influenced by the flame pinch off. Indeed, at the first of these regions the flame surface area is nearly invariant with time, whereas at the second and third regions an unsteady behaviour is seen to arise. In particular, in this figure the ICF initially exhibits an increasing flame surface area, Figs. 9a-9e, due to the rolling up of the flame tip. However, at Fig. 9f, the rolled up flame front collapses, leading to a fast annihilation of the flame surface. This in turn leads to fluctuations of surface area, which are associated to the rapid consumption of the fresh reactant pocket seen in Figs. 9f-9i. Even if this annihilation is cyclic, it should be emphasized that this cycle is not deterministic, as will be seen below, and exhibits some degree of randomness.

In order to further characterize the unforced flame behavior, the flame surface area ($A(t)$) has been obtained as described in section 2.4 and the relative fluctuations A'/\bar{A} are shown at Fig. 10, as well as the corresponding frequency spectrum. Accordingly, Fig. 10a depicts the flame surface area fluctuation, for a period of 300 ms , and Fig. 10b the corresponding FFT. The flame surface oscillating behavior may clearly be seen. The large ($\pm 50\%$) fluctuations of the flame surface area underscore that there are some instants where the flame front has an abrupt reduction which are preceded by a relatively slower increase. These abrupt periodic variations are directly linked with the

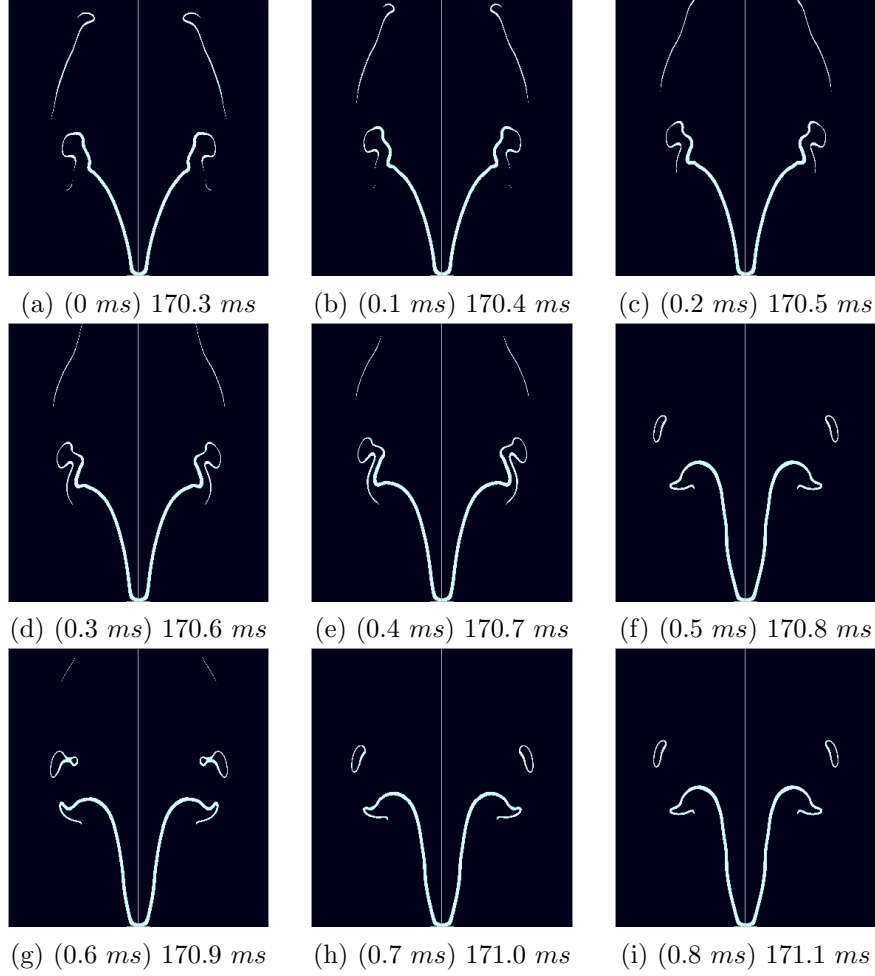
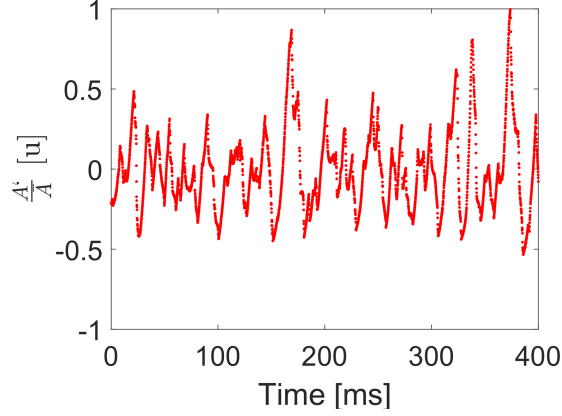


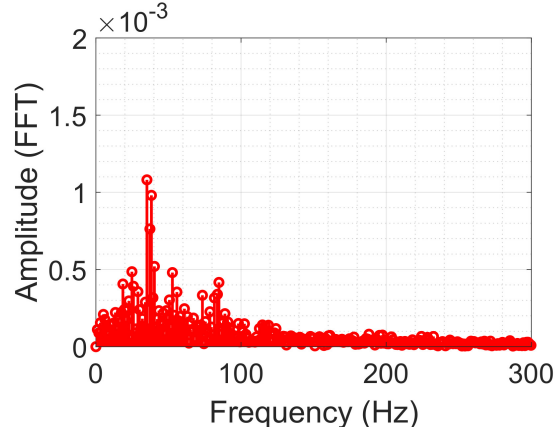
Figure 9.: Unforced flame front position at different equally spaced (by $100 \mu s$) instants in time.

annihilation of the flame front, seen at Fig. 9. Indeed, the maximum observed when $170 \leq t \leq 180 \text{ ms}$ at the flame surface fluctuation (Fig. 10a) lies at the exact moment when the flame surface annihilation begins. Figure 10b shows that the corresponding spectrum features a distinct peak at the frequency of 35 Hz . This suggests that the flame behavior features self-excited oscillations at this natural frequency.

Figure 11a depicts the Fourier spectrum of pressure data obtained at point O (Tab. 1), for a frequency range $f \in [-200, 200] \text{ Hz}$. This figure also suggests that the unforced flame naturally oscillates at a frequency $f = 35 \text{ Hz}$, which further illustrates the claim hypothesized in [9] that the ICF does not have an equilibrium state, or has an unstable one. Figure 10b depicts the corresponding response in time domain. This result is similar for all the points of data extraction presented in Tab. 1 and, for the sake of brevity, only the results for point O are given. Indeed, since all the pressure fluctuation curves are superimposed, the ICF response modeled in this work is acoustically compact [24] which means that the entire flame dynamic response is dictated by its main frequencies.



(a) Unforced ICF relative flame surface area fluctuation.



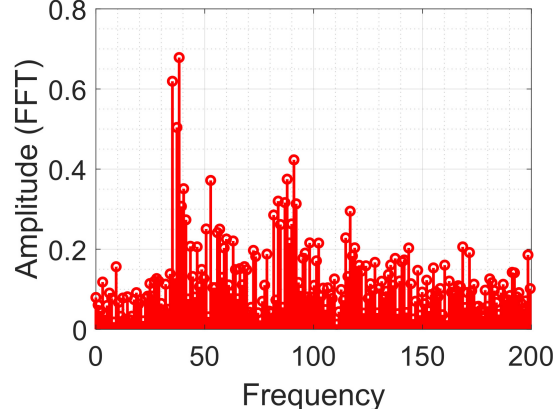
(b) Unforced ICF FFT result.

Figure 10.: Flame surface area response history and frequency behavior.

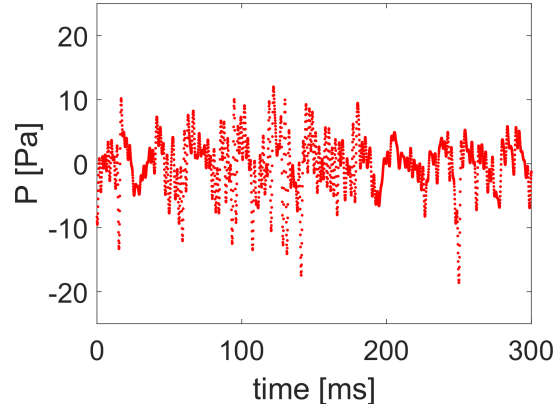
3.1.2. Fluctuating Temperature and OH Mass Fraction

The developed computational model enables the analysis of several flame properties transient behavior. Here, an unsteady analysis of temperature (T) and OH mass fraction (Y_{OH}) is presented. The temperature on premixed flames gives the position of the flame front, where the temperature increases from ambient $T_{\infty} = 300 \text{ K}$ to the flame adiabatic temperature $T_{ad} = 2,200 \text{ K}$. On the chemical kinetic side, the analysis of OH mass fraction, an intermediate species on the combustion process, enables an alternative characterization of the flame front, since this property has its higher concentration on the reactive region, but non-zero values at equilibrium.

Accordingly, fig. 12 depicts the evolution of temperature and OH mass fraction with time, for various locations. The unsteady motion of the flame front is seen with sufficient temporal resolution to adequately capture the passage of fresh and burned gases, i.e., when the temperature varies from $T_{\infty} = 300$ to $2,200 \text{ K}$, while the flame fluctuates across a given measurement (probe) position. Indeed, Fig. 12a shows that each temperature varies between $T_{\infty} = 300 \text{ K}$ at the fresh gases to $T_{ad} = 2,200 \text{ K}$ at the burned gases and vice-versa, such as at the regions where the temperature presents fast variations, e.g. $30 \leq t \leq 42 \text{ ms}$ for point M ($\text{---}\text{O}\text{---}\text{O}\text{---}$), which also indicates the passage of the flame front over the point. The temporal data depicted at Fig.



(a) Unforced ICF pressure FFT result.



(b) Unforced ICF reconstructed pressure data.

Figure 11.: Pressure history frequency analysis and signal reconstruction for the unforced ICF. The depicted results are relative to the data extracted at point O (—), presented at Tab. 1.

12 gives an accurate temporal and spatial characterization of the ICF. The time step $100 \mu s$ is adequate in regard to the time scale of the temperature dynamics, particularly when a high gradient is characteristic of the passage from burned to fresh gases, such as at the period of $2 ms$ (from $T_{\infty} = 300 K$ to $T_{ad} = 2,200 K$), thus showing that the model is able to capture even the intermediary states of the flame, i.e., within the flame front thickness.

Similarly, the evolution of the OH mass fraction at point M features complete passages of the flame front characterized by non-monotonic behavior, whereas points G and O show incomplete passages. Nevertheless, point I (\square) has a constantly zero OH mass fraction, thus being positioned in the fresh gases region.

Moreover, Fig. 12a features an incomplete passage of the flame front over the point M, e.g. at $t = 17 ms$ or $t = 50 ms$, since the temperature curve has extremes in intermediate stages of the temperature ($T_{\infty} < T < T_{ad}$). Such a dynamic characterization of the flame front is indeed distinct from other methodologies, such as the level-set technique that consists in modeling the flame surface with a Damköhler value that tends to infinity, thus segregating the burned from the fresh gases [30]. The temperature data extracted with points G (—) and O (---) exhibits similar trends since the

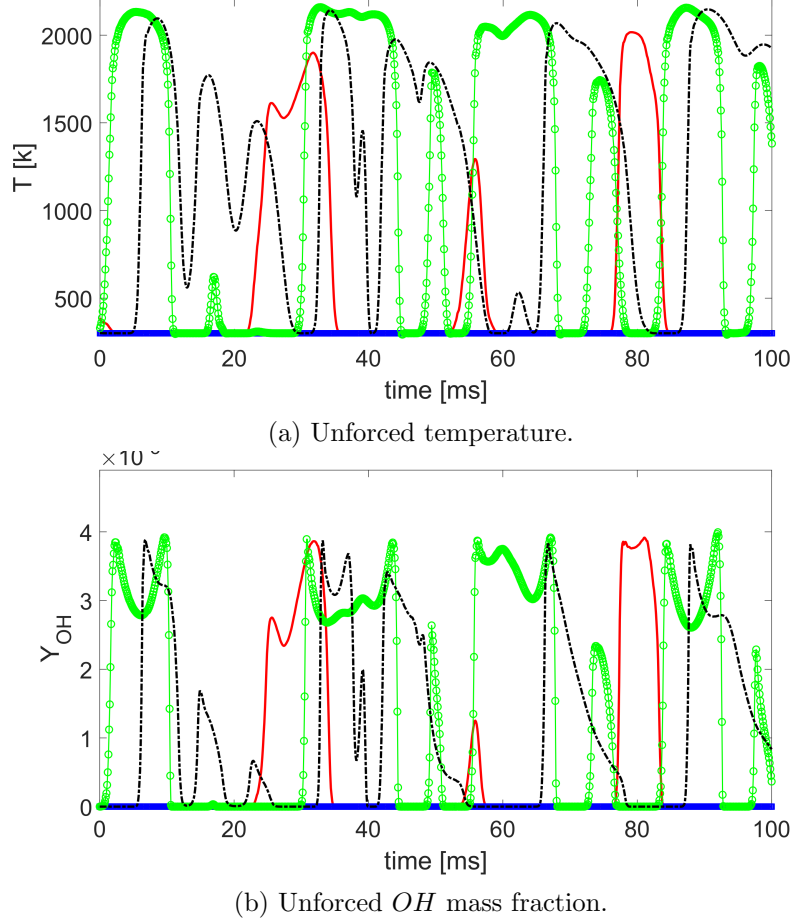


Figure 12.: Temporal fluctuations obtained at 4 different positions, points G (—), I (□), M (○) and O (---), given at Tab. 1.

temperature varies between $T_\infty < T < T_{ad}$ over the time. However, for both points, the temperature does not fully increases across the flame surface, thus not reaching the burned gases region and staying at intermediate temperatures at most of the time.

Moreover, when the burned gases are over the probe, e.g., point M when $30 \leq t \leq 50$ ms at Fig. 12a, the temperature presents a nearly steady behavior, close to the adiabatic flame temperature ($T_{ad} = 2,200$ K) until the flame cross the probe, passing from burned to fresh gases, thus decreasing the temperature. However, concerning now the OH mass fraction (Fig. 12b), when probe is over the burned gases, the behavior is non monotonic. The OH mass fraction reaches a maximum value at the beginning of the reactive region, but this species continues to react with others products, thus decreasing its mass fraction, until the equilibrium is nearly achieved. This is consistent with literature results [9], which underscores the quality of the model.

3.2. Forced flame analysis

This section presents a parametrical study of the harmonically excited ICF. A temperature gradient mesh refinement threshold of 50 K/m is used. Following the results presented with a tighter mesh adaption criteria, one may expect mainly the forcing

response to be recovered such that the natural behavior is seen with less strength. The harmonic excitation is defined by Eq. (1), with a root mean square magnitude of 0.14 m/s , as previously discussed in section 2.1. Different excitation frequencies, varying from 50 Hz to 250 Hz are considered. Such a choice follows that of the experimental studies [4, 10]. In this section, the fluctuation flame structures and the flame surface analysis is presented first, then, the flame describing function is determined.

All the simulations discussed here span at least 400 ms , which is the window used for computing the results for the Fast Fourier Transform and the flame transfer function. Regarding the temperature and OH mass fraction fluctuation of the excited ICF, the behavior has been found to be similar to that of the unforced flame. Therefore, for the sake of brevity, these properties results are not further discussed in this section.

3.2.1. Fluctuating flame structures

Figure 13 gives the flame front instantaneous position for the forcing of $50, 75, 100, 125, 150, 172$ and 200 Hz . The Strouhal number ($St_d = f \cdot (d/\bar{v})$) here has its minimum and maximum values equal to 0.476 and 2.37 , respectively, which are linked to the minimum and maximum exciting frequency of 50 and 250 Hz . Each row corresponds to a different frequency, whereas the elapsed time labels the image shown at each column. The starting time (zero ms) corresponds to the beginning of a cycle, which is defined by the moment where a wrinkle starts developing at the anchor point. A time span of 20 ms is shown, with the flame front depicted at equally spaced intervals of 2.5 ms , thus enabling to present at least one flame response period for each excitation. Note, however, that this image interval choice does not permit to follow flame front behavior corresponding to higher frequencies. In a global comparison and similarly to what has been observed for the unforced flame, the excited flame response may be separated in three regions; (a) the first closer to stabilizing rod, (b) the second one downstream along the flame, where the roll up is seen, and (c) the third at the flame tip, where the pinch-offs are seen.

The flame base response presents a inverted conical shape for all incoming excitations, however, different patterns are seen. In the first three rows ($50, 75$ and 100 Hz), the ICF base oscillates between two different positions, such that a narrow and a wide V-shape are seen. At the first line, e.g., where the ICF is under a forcing of 50 Hz , the instant 0 ms presents a narrow V-shaped, while instant 12.5 ms presents a wide shape. For the larger forcing frequencies, the following four rows ($125, 150, 172$ and 200 Hz), this behavior is not remarked, and the ICF presents a wide V-shape. However, the flame front is wrinkled along its base, as seen at the sixth row, for all instants. These wrinkles are linked to the incoming velocity excitation, and begins at the anchor point of the ICF, at the centered bluff-body, and propagates along the flame front.

The development of the wrinkles along the ICF leads to the flame roll up which dominates the second and the third regions of the flame. The roll up effect is clearly seen for all excited flames, however, it has different shapes. At the flames with incoming velocity forcing frequency varying in $50 \leq f \leq 125 \text{ Hz}$ roll up is easily remarked, e.g., instants 2.5 ms to 5 ms for the incoming forcing of 125 Hz , where the wrinkle starts bending the flame, forming a small bulge which subsequently develops into a roll up. The ICF with incoming forcing ranging from $125 < f \leq 200 \text{ Hz}$, however, has a different roll-up development, since the wrinkles are present along the whole flame front. One may note that, at the seventh row, for 200 Hz , the flame presents a combined behavior, such that the bulge start forming along the flame front and it can be seen initially (as in 0 to 5 ms), but not subsequently (as in 15 to 20 ms).

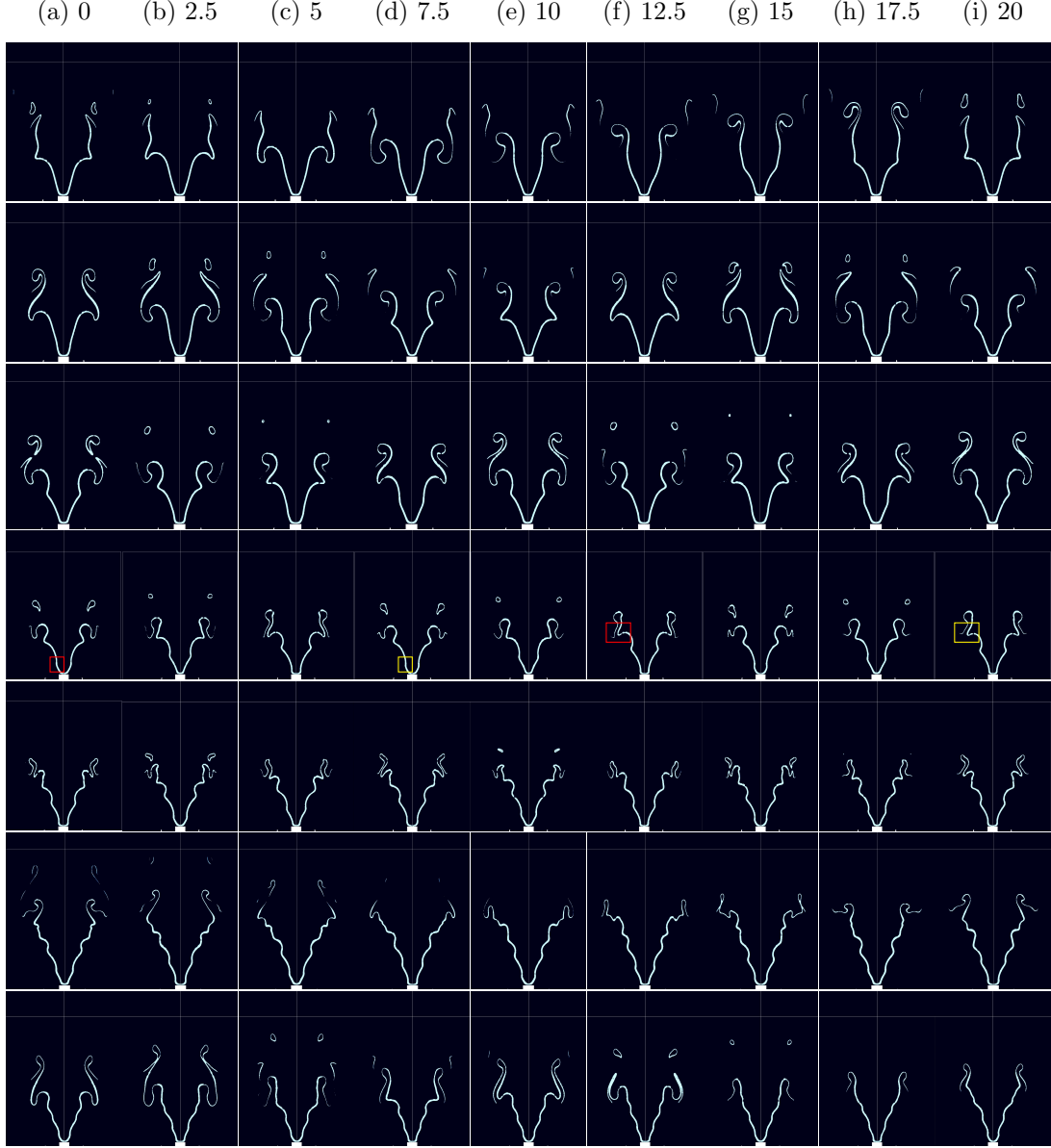


Figure 13.: Flame front surface at different, equally spaced instants (by 2.5 ms), for different forcing frequencies. Each row presents a different forcing frequency, in the following order: 50, 75, 100, 125, 150, 172 and 200 Hz .

Eventually, the roll-up effect at the flame front evolves until the ICF tip is completely bent, such that two sections of the flame collapse, causing the annihilation of the respective section and creating a pinch off. This phenomenon is seen at the ICF for all incoming excitations, with some variations, characterizing the last third of the ICF. The forcing frequencies ranging from 50 to 125 Hz yield a well defined pinch off, as shown at the second row (75 Hz), 15 ms . Nonetheless, the ICF response to higher frequencies (125 to 200 Hz) has a slightly smaller and less intensive pinch off, when compared to lower frequencies, such as seen at the sixth row (172 Hz) for instants 12.5 to 15 ms . Again, the flame response to 200 Hz (seventh row) presents a mixed behavior, which could be linked to the fact that this forcing is an harmonic of the

100 Hz frequency.

Moreover, Fig. 13 actually also suggests a general classification of the ICF response in terms of similar behavior; the behavior (1) due to low frequency forcing, at the first to the fourth rows, from 50 to 125 Hz , and (2) due to high frequency excitation, from the fifth to the seventh row. For instance, the first class is characterized by the ICF responding only to the incoming excitation, and all phenomena are linked to the frequency of the forcing. The second class corresponds to a mixed response, such that the flame behavior due to the incoming forcing and the flame natural behavior are interacting, at a frequency around 40 Hz .

In addition, it has also been noted that the ICF response to incoming velocity excitation of 125 Hz ($S_{td} = 1.35$) has a smaller flame length (and thus surface area) when compared to response to other forcing frequencies. This effect is a result of the velocity of the propagation of the wrinkles, which travel along the ICF, causing the roll up and pinch off of the flame front, faster than the velocity which the flame takes to naturally develop itself. Indeed, at the fourth row of Fig. 13 the wrinkle travels from the flame anchor point, e.g. the red box at 0 ms , to the instant where it interferes with the bulge formation, e.g. the red box at 12.5 ms , exhibiting a propagation time of ≈ 12.5 ms . Moreover, while the first wrinkle (red box) propagates, a new wrinkle starts forming (yellow box at 7.5 ms), due to the excitation frequency. The second wrinkle (yellow box) then travels along the flame, until it interferes with a bulge, as shows the yellow box at 20 ms . In effect, the wrinkle propagation time is 14 ms , such that its frequency is ≈ 62.5 Hz , which is also an harmonic of the forcing frequency of 125 Hz , creating a constructive interference between both phenomena and causing the ICF length reduction.

3.2.2. Flame surface area fluctuation frequency analysis

To quantify the dynamic behavior of the flame, similarly to what has been performed in the unforced case, the flame surface area fluctuations are analyzed for different incoming excitations, as depicted at Fig. 14. The corresponding frequency domain analysis is developed for each of these signals, using a FFT, such that the response of the ICF is obtained and compared to the incoming velocity harmonic excitation. These results are given in Fig. 15.

From the flame surface area fluctuation analysis, four different flame behaviors are found to arise, depending on the incoming excitation frequency. Therefore, for the sake of brevity, only one example of each behavior is given in Fig. 14. First, the flame presents an oscillating behavior associated to the forcing, and some of its harmonics, as suggests the two different type of excursions at Fig. 14a. The second behavior is marked only by the forcing frequency, such as when $f = 100$ Hz , as Fig. 14b depicts. The third behavior, seen at Fig. 14c, the flame responds to the incoming forcing frequency and exhibits other frequencies. The flame surface response due to higher frequencies incoming excitation ($f > 150$ Hz), corresponding to the fourth flame behavior, is not disturbed by the forcing frequency, but presents a nonlinear response that does not suggests any visual classification, as depicted at Fig. 14d where $f = 200$ Hz . The corresponding FFT results of the flame surface area fluctuation behavior are presented at Fig. 15.

As it was expected from the experiments, the ICF is characterized by a remarkable harmonic response to the incoming excitation, and its behavior depends on the forcing frequency. This is now examined by considering the frequency domain response of the flame surface area to the incoming forcing, depicted at Fig. 15. It is noteworthy that

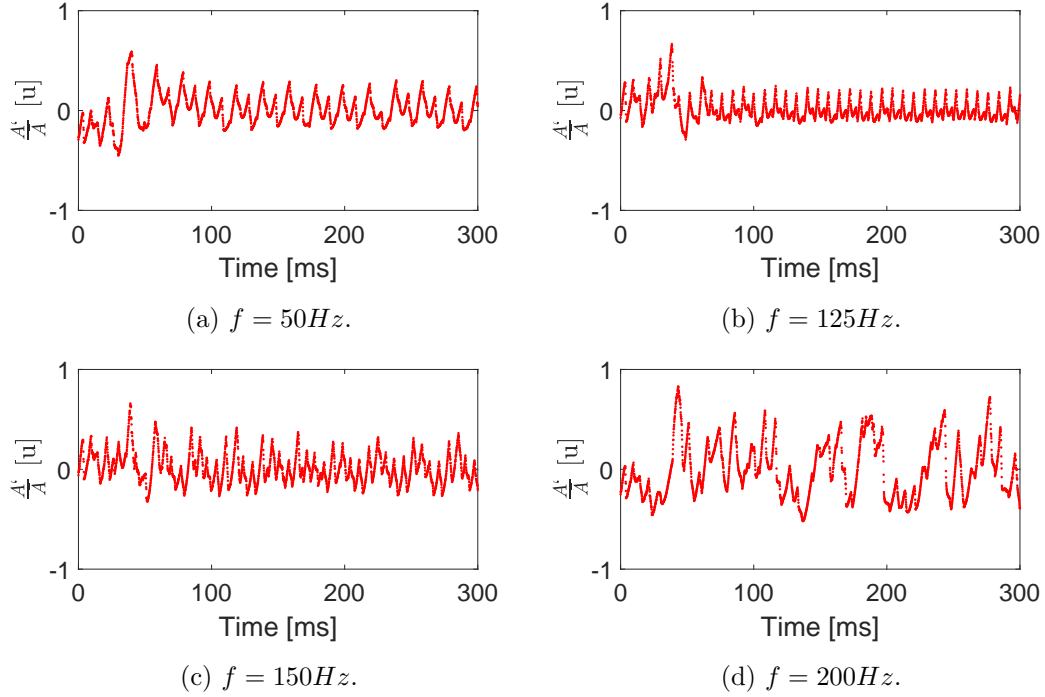


Figure 14.: Flame surface area fluctuation due to different incoming forcing frequencies.

the velocity forcing is harmonic immediately upstream to the flame, for all forcing frequencies. The flame surface response at frequencies $f = 50$ and 125 Hz , Figs. 15a and 15d respectively, are marked by the incoming excitation, having its energy concentrated at its respective forcing frequency. Also, a few harmonics of the forcing are seen to be as strong as the excitation, as shows Figs. 15a and 15d, at $f = 100 \text{ Hz}$ for the first excitation and 250 Hz for the second. Other flame surface responses also exhibit harmonics of the forcing excitation, but with a significantly smaller amplitude, such as for an excitation of $f = 100 \text{ Hz}$ (Fig. 15c), where is is worth to note that the highest gain is expected from experiments. In addition, when the forcing frequency increases to $f = 150 \text{ Hz}$, significantly different behavior arises: a mix between the forcing and low frequencies may be seen at Fig. 15e, with a remarkable flame response around $f = 35 \text{ Hz}$ and one at $f = 150 \text{ Hz}$, where the first frequency remarks the natural behavior of the ICF. Then, for $f \geq 172 \text{ Hz}$, depicted at Figs. 15f-15h, the ICF response to the incoming excitation is characterized by a low magnitude, which is also associated be the flame natural harmonic behavior, and also by a broadband amplitude signal.

Unfortunately, the available experimental results [4, 28] does not include such detailed flame surface area data as that presented here, nor the full spectral analysis. However, since the flame spectral response seems to significantly vary with the forcing frequency, it could be interesting to revisit this flame with diagnostics able to perform a time resolution of the flame surface.

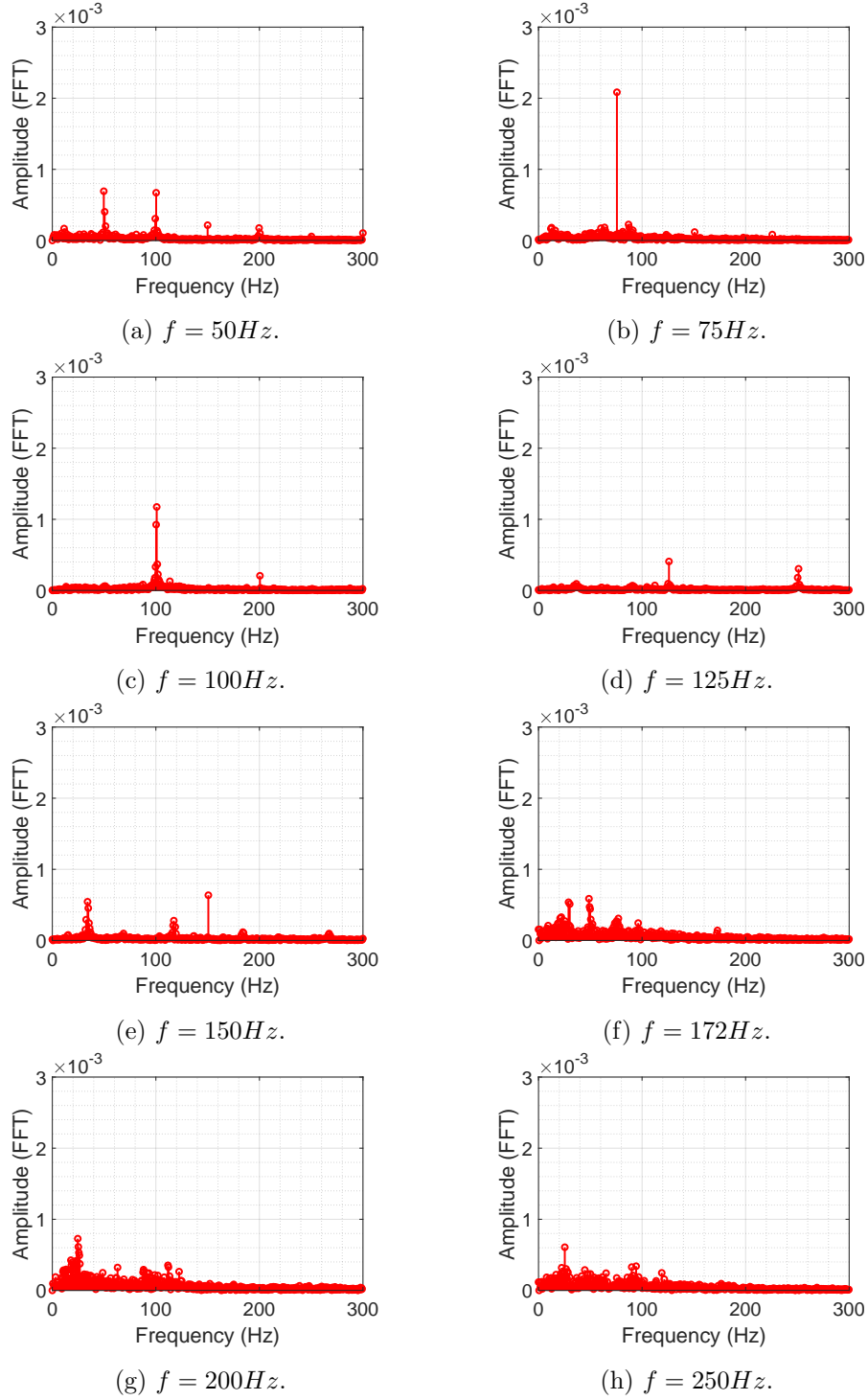
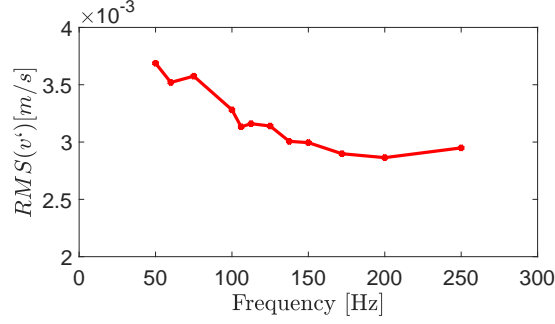


Figure 15.: Harmonic response of the flame surface area fluctuation for different forcing frequencies (f).

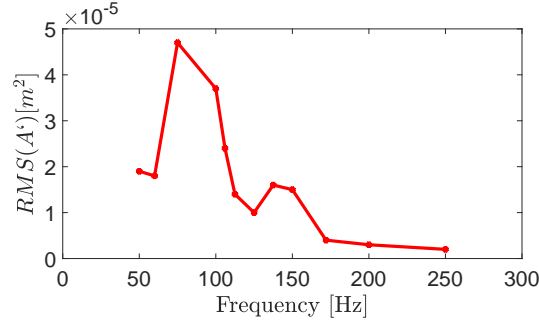
3.2.3. Flame transfer function

A direct comparison between the experimental and numerical results is nevertheless possible by considering the FTF, which has been computed based on the gain defined

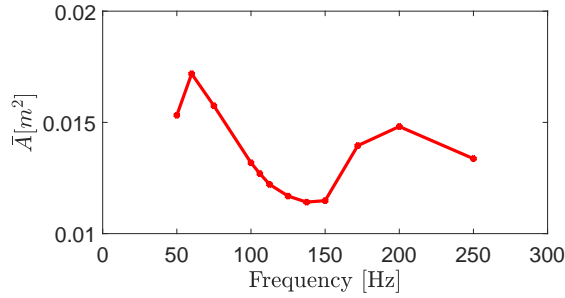
at section 2.4. Here the gain of the ICF due to different incoming velocity fluctuations is shown for different frequencies f . Accordingly, at Fig. 16, the root mean square of the velocity ($RMS(v')$) and flame surface area fluctuations ($RMS(A')$), followed by the mean of the flame surface area (\bar{A}) are given in function of frequency, whereas, the gain and phase of the ICF as a function of the frequency is given and compared to experimental data in Fig. 17.



(a) RMS(v').



(b) RMS(A').



(c) Mean(A).

Figure 16.: Dependency of the RMS of the inlet velocity fluctuation, RMS and mean of the flame surface area fluctuation with the incoming forcing frequency.

The RMS of the velocity fluctuation immediately upstream to the flame, shown in Fig. 16a exhibits a decreasing trend with frequency. Such a decrease is associated to

the boundary layer thickness decrease with frequency predicted by the solution of the second Stokes problem [?]. Conversely, the larger flow cross section blockage due to thicker boundary layers at lower forcing frequencies leads to larger core flow velocity fluctuations.

The RMS of the flame surface area fluctuation (fig. 16b) presents a maximum value for a frequency of 75 Hz , and it decreases until it achieves a value of $\approx 4 \times 10^{-5} \text{ m}^2$, and also, sudden a drop close to 125 Hz is seen to arise. The mean surface area also varies remarkably (Fig. 16c), such that its maximum is around 60 Hz , and it decreases for frequencies $75 < f < 150 \text{ Hz}$, where it stabilizes, remaining almost constant $\approx 0.3 \times 10^{-5} \text{ m}^2$. The decrease on the \bar{A} is linked to the length of the inverted conical flame front, which decreases due to the interference between the forcing frequency and the wrinkle propagation time, as already discussed in section 3.2.2.

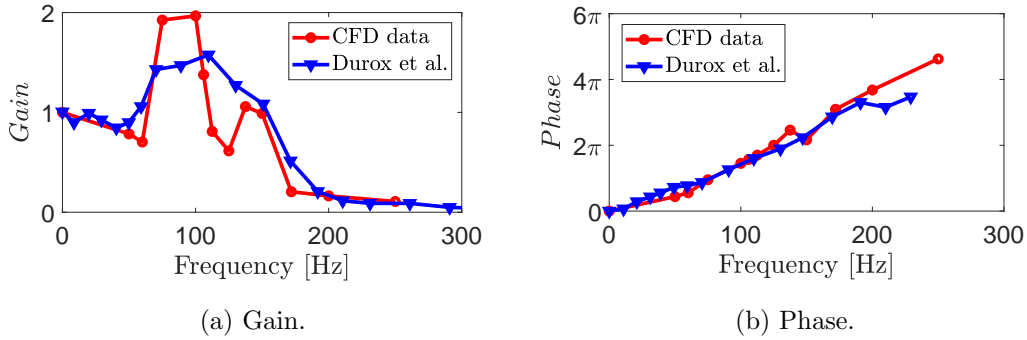


Figure 17.: Gain and phase difference between velocity and flame surface area fluctuation of the ICF as a function of the incoming forcing frequency.

The gain, given at Fig. 17a, shows a behavior similar to the experimental results [10]. The gain tends to 1 for low frequencies ($f \leq 60 \text{ Hz}$), and it increases when forcing between $75 \leq f \leq 125 \text{ Hz}$, reaching its maximum values at $f = 100 \text{ Hz}$. One may note that the computed gain exhibits a maximum value that is higher than the experimental one, which, as previously discussed, is associated to the mesh refinement threshold choice, that balances the computational cost with respect to model accuracy. Furthermore, the gain decreases between $106 < f \leq 150 \text{ Hz}$, achieving 0.7 for $f = 125 \text{ Hz}$, which is linked to the flame surface area fluctuations suppression due to the wrinkle interference. For higher frequencies, $f \geq 150 \text{ Hz}$, the model and experiments yield a remarkably close agreement, one for which the gain decreases with frequency. Finally, the phase seen at Fig. 17b, presents a similar behavior to experimental results, where the phase difference between velocity and flame surface area fluctuation increase linearly with frequency.

4. CONCLUSION AND PERSPECTIVES

The unsteady models of the inverted methane-air conical flame (ICF), developed with Fluent 2019/2020, show that it is possible to compute for such complex physical, thermo-acoustic and reactive system, allowing the further understanding of the flame dynamic behavior. The use of a skeletal kinetic chemical model enables the analysis of diverse species, thus also allowing the instantaneous characterization of the flame front an its surface by means, in particular, of CH_2 and OH mass fraction . The analysis of

the flame structures showed that the behavior of ICF is marked by instabilities in the unforced and forced situations, being characterized by the roll up of the flame front till the annihilation of a section of the flame tip, agreeing with existing experimental results.

The mesh adaption analysis shows that the variation of the corresponding temperature gradients thresholds enables the characterization of the ICF natural and forced behavior. However, the choice of those thresholds must carefully be considered. Indeed, the use of a tight refinement adaption threshold of 10 K/m leads to the characterization of the complete flame front behavior, but with a prohibitive computational cost. Relaxing the refinement threshold to 50 K/m , nevertheless, enables the modeling of the flame fluctuation behavior, at all regions, i.e., base, pinch off and wrinkles, but with an acceptable burden.

The analysis of temperature, pressure and mass fraction of OH fluctuation behavior enabled the characterization of the flame front dynamic response to incoming velocity fluctuations. Moreover, the results were analyzed in terms of the different time and space scales. It was shown that not only the flow of the substances but the fast dynamic movement of the flame front inner structure is also captured, which differs from other methodologies, such as the level-set technique [30].

The flame front dynamic analysis enabled the detailed characterization of the impact of the forcing on the ICF shape. The flame has been shown to exhibit three main regions: (1) the base that has a conical V-shape that oscillates between narrow and wide, and where the development of the wrinkles are seen, (2) the roll up region further downstream the flame and (3) the flame tip, where the flame annihilation happens. Each of these regions is impacted differently by the incoming excitation Strouhal number, i.e., the flame base presents oscillating behavior between wide and narrow V-shape $0.47 \leq S_{td} < 1.19$, and it switches to a steady wide V-shaped flame when $S_{td} \geq 1.43$.

Moreover, the roll up region (2) responds similarly to the various forcing frequencies, such that the flame rolls up until annihilation. However, the position where the roll up happens changes with the forcing, being in a earlier stage when the Strouhal number is such that $S_{td} \leq 1.19$, and in a later stage otherwise. The third region, where the flame tip pinch off is observed, also has shown similar behavior for most cases, i.e., all forced ICFs present the annihilation of the flame front at a given instant, and this phenomena happens at the forcing period for $S_{td} \leq 1.19$, but not in synchronized time when $S_{td} \geq 1.43$. This loss of the synchronization effect is attributed to the interaction between the flame natural behavior with the ICF response due to the external excitation. Nevertheless, when $S_{td} = 1.19$, a remarkable reduction (20%) on the flame length is caused by the interaction of the wrinkle and the pinch off, impacting also on the flame surface area fluctuation and, as a consequence, on the gain.

The frequency analysis of the excited flame surface area fluctuation underscores the multiple behaviors of the flame due to forcing with different frequencies. For instance, the behavior when $S_{td} = 0.48$ shows a strong response due to the forcing and its second harmonic, however, when $0.71 \leq S_{td} \leq 0.95$, the flame behavior is only due to the forcing excitation. In addition, when forcing around $S_{td} \approx 1.43$, the flame presents a mixed response caused by the incoming velocity fluctuation which interacts with the flame low frequency natural behavior of $f = 35\text{ Hz}$ ($S_{td} = 0.33$). Higher frequency excitations, $S_{td} > 1.43$, do not present any response due to the forcing, but has a strong natural response, characterized by the low broadband frequency $f \leq 35\text{ Hz}$. Furthermore, the frequency analysis enables the characterization of ICF thermo-acoustic response by means of FTF gain and phase.

The gain obtained by the computational model agrees with the experimental results. However, two main discrepancies were found; first, the maximum gain has higher value ($G = 2$) than at frequencies $f = 75, 100 \text{ Hz}$ as a result of the choice of mesh adaption refinement gradient threshold of 50 K/m . Besides, a decrease on the gain is seen for $100 < f \leq 125 \text{ Hz}$, achieving $G = 0.8$, and this behavior is a consequence of the interference between wrinkles and pinch offs at the flame front. Moreover, the FTF phase shows remarkable agreement with the experiments.

This study enabled a detailed characterization of the ICF and its flame surface area and its full spectral analysis, which has not been included by experimental analysis [4, 10, 12, 23]. This paper shows that the flame surface response due to the velocity excitations significantly varies with the forcing, presenting different behaviors, and it would be interesting to revisit the experiments with methodologies that enable a more detailed characterization of the flame.

Finally, the successful modeling and characterization of the ICF and its flame response to incoming velocity excitations open doors to the development of the modeling of the flame describing function with different approaches, such as machine learning methods. Since the unsteady CFD model of the ICF is created and validated, the next step then is to use the different optimization models to compute the FDF gain and phase, allowing the complete frequency characterization of the ICF with lower computational cost.

5. ACKNOWLEDGMENTS



This project has received funding from the European Union's Horizon 2020 research and innovation programme under grant Agreement nr 766264. This work was performed while L.F. Figueira da Silva was on leave from the Institut Prime (CNRS, France). The authors also gratefully acknowledge the support provided by Conselho Nacional de Desenvolvimento Científico e Tecnológico, CNPq, under the Research Grant No. 403904/2016-1.

References

- [1] J. Shinjo, Y. Mizobuchi, and S. Ogawa, *Numerical simulation of flame behavior in a lean premixed gas turbine combustor*, in *Combustion and Noise Control*, G.D. Roy, ed., Cranfield University Press, Cranfield, UK, 2003, p. 9.
- [2] P. Gobatto, M. Masi, A. Lazzaretto, and A. Toffolo, *Analysis of the natural acoustic modes of a gas turbine combustor using isothermal cfd simulations*, *Applied Thermal Engineering* 126 (2017), pp. 489–499.
- [3] J. van Oijen, A. Donini, R. Bastiaans, J. ten Thijs Boonkamp, and L. de Goey, *State-of-the-art in premixed combustion modeling using flamelet generated manifolds*, *Progress in Energy and Combustion Science* 57 (2016), pp. 30–74.
- [4] A.L. Birbaud, D. Durox, S. Ducruix, and S. Candel, *Dynamics of confined premixed flames submitted to upstream acoustic modulations*, *Proceedings of the Combustion Institute* 31 (2007), pp. 1257–1265.
- [5] A. Coimbra and L.F. Figueira da Silva, *Modelling of a turbulent lean premixed combustor using a Reynolds-Averaged Navier–Stokes approach*, *Journal of the Brazilian Society of Mechanical Sciences and Engineering* 42 (2020).
- [6] N. Noiray, D. Durox, T. Schuller, and S. Candel, *A unified framework for nonlinear*

- combustion instability analysis based on the flame describing function*, Journal of Fluid Mechanics 615 (2008), pp. 139–167.
- [7] T. Lieuwen and K. McManus, *Combustion dynamics in lean-premixed prevaporized (LPP) gas turbines*, Journal of Propulsion and Power 19 (2003), pp. 721–721.
 - [8] V.D. Milosavljevic, *Perturbation in combustor near-field aerodynamics as a main source of thermoacoustic instabilities in modern industrial dry low NO_x gas turbine combustion systems*, in *Combustion and Noise Control*, G.D. Roy, ed., Cranfield University Press, Cranfield, UK, 2003, pp. 55–60.
 - [9] L. da Costa Ramos, F. Di Meglio, L.F. Figueira Da Silva, and V. Morgenthaler, *Reduced order model of laminar premixed inverted conical flames*, in *AIAA Scitech 2020 Forum*, 2020.
 - [10] D. Durox, T. Schuller, and S. Candel, *Combustion dynamics of inverted conical flames*, Proceedings of the Combustion Institute 30 (2005), pp. 1717–1724.
 - [11] *Dynamics and stability of lean-premixed swirl-stabilized combustion*, Progress in Energy and Combustion Science 35 (2009), pp. 293–364.
 - [12] S. Ducruix, D. Durox, and S. Candel, *Theoretical and experimental determinations of the transfer function of a laminar premixed flame*, Proceedings of the Combustion Institute 28 (2000), pp. 765 – 773.
 - [13] T. Schuller, S. Ducruix, D. Durox, and S. Candel, *Modeling tools for the prediction of premixed flame transfer functions*, Proceedings of the Combustion Institute 29 (2002), pp. 107–113.
 - [14] L. Boyer and J. Quinard, *On the dynamics of anchored flames*, Combustion and Flame 82 (1990), pp. 51 – 65.
 - [15] A.P. Dowling, *A kinematic model of a ducted flame*, Journal of Fluid Mechanics 394 (1999), p. 51–72.
 - [16] C. Li, M. Zhu, and J.P. Moeck, *An analytical study of the flame dynamics of a transversely forced asymmetric two-dimensional bunsen flame*, Combustion Theory and Modelling 21 (2017), pp. 976–995.
 - [17] F. Baillot and F. Lespinasse, *Response of a laminar premixed v-flame to a high-frequency transverse acoustic field*, Combustion and Flame 161 (2014), pp. 1247 – 1267.
 - [18] E. Luciano and J. Ballester, *Analysis of the dynamic response of premixed flames through chemiluminescence cross-correlation maps*, Combustion and Flame 194 (2018), pp. 296 – 308.
 - [19] D. Michaels and A.F. Ghoniem, *Leading edge dynamics of lean premixed flames stabilized on a bluff body*, Combustion and Flame 191 (2018), pp. 39 – 52.
 - [20] S. Jaensch, M. Merk, T. Emmert, and W. Polifke, *Identification of flame transfer functions in the presence of intrinsic thermoacoustic feedback and noise*, Combustion Theory and Modelling 22 (2018), pp. 1–22.
 - [21] X. Han, J. Li, and A.S. Morgans, *Prediction of combustion instability limit cycle oscillations by combining flame describing function simulations with a thermoacoustic network model*, Combustion and Flame 162 (2015), pp. 3632 – 3647.
 - [22] T. Pant, C. Han, and H. Wang, *Computational investigations of the coupling between transient flame dynamics and thermo-acoustic instability in a self-excited resonance combustor*, Combustion Theory and Modelling 23 (2019), pp. 854–884.
 - [23] T. Steinbacher, A. Albayrak, A. Ghani, and W. Polifke, *Consequences of flame geometry for the acoustic response of premixed flames*, Combustion and Flame 199 (2019), pp. 411 – 428.
 - [24] W. Polifke, *Modeling and analysis of premixed flame dynamics by means of distributed time delays*, Progress in Energy and Combustion Science 79 (2020), p. 100845.
 - [25] A. Kazakov and M. Frenklach (eds.), *Reduced Reaction Sets based on GRI-Mech 1.2*, <http://combustion.berkeley.edu/drm/>, Berkeley, CA 94720-1740, USA, 1984.
 - [26] C. Celis and L.F. Figueira da Silva, *Computational assessment of methane-air reduced chemical kinetic mechanisms for soot production studies*, Journal of the Brazilian Society of Mechanical Sciences and Engineering 38 (2016), pp. 2225–2244.

- [27] W. van Drongelen, *Chapter 6 - continuous, discrete, and fast fourier transform*, in *Signal Processing for Neuroscientists*, W. [van Drongelen], ed., 2nd ed., Academic Press, 2018, pp. 103 – 118.
- [28] S. Ducruix, T. Schuller, D. Durox, and S. Candel, *Combustion dynamics and instabilities: Elementary coupling and driving mechanisms*, *Journal of Propulsion and Power* 19 (2003), pp. 722–734.
- [29] B. Lewis and G. Von Elbe, *Combustion, flames, and explosions of gases*, 3rd ed., Academic Press, 1987.
- [30] T. Poinso and D. Veynante, *Theoretical and numerical combustion*, 2nd ed., Edwards, 2005.